Deformable Registration of Glioma Images Using EM Algorithm and Diffusion Reaction Modeling

Ali Gooya*, *Member, IEEE*, George Biros, *Member, IEEE*, and Christos Davatzikos, *Senior Member, IEEE*

***Abstract*—This paper investigates the problem of atlas registration of brain images with gliomas. Multiparametric imaging modalities (T1, T1-CE, T2, and FLAIR) are first utilized for segmentations of different tissues, and to compute the posterior probability map (PBM) of membership to each tissue class, using supervised learning. Similar maps are generated in the initially normal atlas, by modeling the tumor growth, using reaction-diffusion equation. Deformable registration using a demons-like algorithm is used to register the patient images with the tumor bearing atlas. Joint estimation of the simulated tumor parameters (e.g., location, mass effect and degree of infiltration), and the spatial transformation is achieved by maximization of the log-likelihood of observation. An expectation-maximization algorithm is used in registration process to estimate the spatial transformation and other parameters related to tumor simulation are optimized through asynchronous parallel pattern search (APPSPACK). The proposed method has been evaluated on five simulated data sets created by statistically simulated deformations (SSD), and fifteen real multichannel glioma data sets. The performance has been evaluated both quantitatively and qualitatively, and the results have been compared to ORBIT, an alternative method solving a similar problem. The results show that our method outperforms ORBIT, and the warped templates have better similarity to patient images.**

***Index Terms*—Brain tumor, deformable registration, expectation-maximization (EM) algorithm, reaction-diffusion equation, statistical atlas, tumor growth modeling.**

NOMENCLATURE:

$(\delta_i^{(m-1)})^{-2}$	Velocity vector norm penalizer at voxel i and iteration m.
λ	Small constant employed for outlier detection.
ψ	Arbitrary test function used to derive the update equation.
$\mathbf{h}i^{(m-1)}$	Deformation field vector at voxel i and iteration m.
$\mathbf{q}$	Set of tumor parameters needed for tumor simulation.
$\mathbf{r}_i^{(m-1)}$	Residual vector used in linear system at voxel i.
$\mathbf{S}_0^{-1}$, $\mathbf{S}_1^{-1}$	Variance matrices of class 0 and 1.
$\mathbf{u}$	Mass-effect deformation field.
$\mathbf{v}_i$	Velocity field vector at voxel i.
$\mathbf{W}_i^{(m-1)}$	Coefficients matrix of linear system at voxel i.
$\mathbf{y}_\mathbf{i}^\mathbf{q}$	Observation vector at ith voxel in Ω_F made by differencingtarget and warped PBMs.
$\mathbf{Y}^\mathbf{q}$	Set of N i.i.d observation difference vectors.
Ω_F	Domain of fixed (patient) PBMs.
Ω_M	Domain of moving (atlas) PBMs.
Φ	Set of unknown parameters to be estimated by EM.
π_0, π_1	*A priori* probability maps for class 0 and 1.
ρ	Proliferation coefficient.
σ_j^{-2}	Variance of jth difference channel.
$C^\mathbf{q}$	Simulated tumor density map.
D_0, D_1	Subregions of Ω_F.
D_{WM}, D_{GM}	Diffusion coefficients of white and gray matter.
f_0, f_1	Probability distribution functions.
F_j	jth fixed (patient) PBM.
F_{simj}	jth simulated target PBM for the purpose of validation.
$M_i^\mathbf{q}$	ith moving PBM generated in atlas.
N	Number of voxels in Ω_F.
p_1, p_2	Mass-effect parameters.
$w_{ik}^{(m)}$	Robust posterior probability of voxel i belonging to class k at iteration m.
x, y, z	Tumor seed coordinates.

Manuscript received July 08, 2010; revised September 11, 2010; accepted September 11, 2010. Date of publication September 27, 2010; date of current version February 02, 2011. This work was supported by National Institute of Health Grant 5R01NS042645. *Asterisk indicates corresponding author.*

*A. Gooya is with the Section of Biomedical Image Analysis, Department of Radiology, University of Pennsylvania, Philadelphia, PA 19104 USA (e-mail: ali.gooya@uphs.upenn.edu).

C. Davatzikos is with the Section of Biomedical Image Analysis, Department of Radiology, University of Pennsylvania, Philadelphia, PA 19104 USA (e-mail: christos.davatzikos@uphs.upenn.edu).

G. Biros is with the College of Engineering Biomedical Engineering, Georgia Institute of Technology, Atlanta, GA 30332 USA (e-mail: biros@gatech.edu).

Color versions of one or more of the figures in this paper are available online at http://ieeexplore.ieee.org.

Digital Object Identifier 10.1109/TMI.2010.2078833

I. INTRODUCTION

GLIOBLASTOMA multiforme (GBM), a primary malignant brain tumor, is the most common form of the glioma tumors, which in spite of multimodality treatments, remains as

an incurable and rapidly fatal disease. The anatomic location of a glioma influences prognosis and treatment options. A few studies aim at discovery of the distribution of gliomas in different anatomic areas of the brain. For instance, Larjaavara *et al.* [1], demonstrate that such distribution of location of gliomas is an uneven function within the brain, with the densest occurrence in the frontal lobe. Duffao *et al.* [2] find that low grade gliomas are often observed in secondary functional areas of the brain. While in these works, manual localization of glioma (in standard space) has been utilized, a deformable registration framework can be very useful for objective numerical evaluations of such clinical findings since various patient images can be mapped to a common space or atlas. Such an statistical atlas derived from glioma images can be a powerful tool for summarizing the population data, examining the spatial relationships between pathology and other anatomical locations, knowledge discovery and learning of glioma behavior.

Although a plethora of methods for normal-to-normal brain registration exist [3]–[17], the problem of registering images of tumor patients to standardized templates has been relatively unexplored, and proven to be extremely challenging. Due to large deformations and lack of clear definition of anatomical detail in patients images, direct application of the available registration methods to images of tumor patients can lead to poor registration around the tumor region. In most of glioma bearing MR images, the confounding effects of edema and tumor inltration, which cause changes in the image intensities, render the task of finding correspondences difficult. In fact, the fundamental assumption of existence of correspondences between the atlas and the patients images, which is ubiquitous in the most of the available deformable registration methods, is violated due to the anatomical changes caused by tumor emergence and tissue death. Another difficulty, is the presence of the mass-effect in the patient image. Mass-effect causes deformations of the adjacent structures and ventricles by excessive pushing, rendering it difficult to apply standard image warping algorithms.

This paper presents a framework to circumvent these difficulties by building upon our work in [18] and [19], i.e., creating a topologically equivalent atlas by simulating tumor in the atlas space and use it for registration to patient images. The parameters of this tumor simulation are estimated as part of the registration process. Apart from methodological details, one feature that is different in our method compared to [18] and [19], is the tumor type studied here. The method in [18] and [19] used a simple pressure model to simulate the tumor mass-effect on the atlas and did not consider tumor infiltration and presence of edema, the most important issues in glioma patients, which are the focus herein. The glioma images usually indicate severe complexities around the tumor and may include edemas that render the registration task extremely challenging. To the best of our knowledge, this work represents the first report of such registration task in the literature.

As in [18] and [19], we capture the total deformation (between atlas and patient's image) using two different components: the mass effect, and the deformation due to the inter-subject differences. Explicit mass-effect simulation by biophysical models [20]–[22] is performed in the atlas space prior to warping to target patient image, thereby allowing more realistic warps to be achieved via image warping. Furthermore, other information such as estimated tumor density can be directly used to compute similarities to the patient images.

A. Related Work

A few publications have proposed the spatial normalization of pathological brain images. Masking of pathologies is utilized in Brett *et al.* [23] and Stefanescu *et al.* [24] where the warping close to tumors is only driven by the information of the neighboring structures. Nowinski *et al.* [25] use feature points (Talairach transformation), followed by a radial mass-effect model to warp atlas onto the patient image. In order to create topologically equivalent pair of images, Kyriacou *et al.* [26] remove the tumor from the patient image, other methods embed a tumor in the atlas (atlas seeding). Atlas seeding has also the advantage that allows more realistic warping, in the form of mass-effect, to be captured. In these methods, a deformation field is first created by mass-effect models, e.g., simplified radial growth models [25], [27], and later refined by a nonrigid deformation based on optical flow [28]–[30]. Incorporation of more advanced biomechanical models of the tumor growth to simulate tissue loss and compute displacements, was introduced in a series of previous publications by our group. For instance Mohamed *et al.* [31], [32], developed a PCA based statistical method to learn the tumor-growth deformations across different subjects, or within the same subject [18]. The statistical approach was chosen to reduce the high computational cost of the finite element based biomechanical models for tumor growth simulation leaving the burden of simulations to offline training. Statistical models, however, are not very accurate and also are limited by the parameters used during training.

Recently, Zacharaki *et al.* proposed ORBIT [18], [19]. Similar to our framework, ORBIT simulates the tumor growth and mass-effect on the atlas prior to warping to the patient image, and it also estimates the best parameter set for this simulation. As ORBIT is originally designed to work with tumors with minimal edema and infiltration, tumor simulation is achieved using the pressure model described in [22], a framework which models tissue necrosis and its replacement by the tumor and also computes the mass-effect. As a result ORBIT, only estimates seed location and the tumor growth factor as the required parameter set.

In contrast to ORBIT, the primary objective of this work is the registration of brain images with GBM, a particular kind of primary tumors which is known to be infiltrative. The tumor may take on a variety of appearances, depending on the amount of hemorrhage, necrosis, or its age and might indicate no clear edges. Mass effect from the tumor and edema may compress the ventricles. Therefore, images with GBM usually have complex and inhomogeneous imaging patterns, which can not be appropriately simulated using the simple pressure tumor model as done in ORBIT.

This paper, proposes a new framework to handle some of these complexities through the following elements.

1) As illustrated in [33], using multimodality MR imaging and supervised SVM based classification, the original intensity data is transfered into the space of the probability

maps (PBMs) of various tissue types, which can be viewed as the memberships to normal and abnormal tissue classes.

2) A more realistic biomechanical tumor model [20] appropriate for GBM, is integrated to our registration framework, and the relevant parameters for the tumor growth modeling (such as seed location, diffusion coefficients, etc.) are estimated. Given an atlas and its corresponding set of healthy tissue probability maps, the estimated tumor density map and the mass-effect is used for explicit computation of the PBMs in the atlas space, allowing the similarities between the corresponding PBMs of the patient and atlas to be measured.
3) We anticipate that the edema can not be estimated through the diffusion-reaction based modeling of tumor growth in [20]. Presence of vasogenic cerebral edema depends on the intracranial pressure gradient and involves complex mechanisms where the bulk flow and not diffusion should be considered as the main cause for the spread of edema through the white matter [34]. The proposed method is capable of handling the lack of edema and such unrealistic molding issues, through the segmentation of the patient space into three different regions roughly as edema, nonedema, and outliers (with respect to registration model).

Because no *a priori* information about the tumor parameters and the registration is given, our problem of joint estimation of the warping, tumor growth parameters and the segmentation labels, is an *estimation problem from incomplete data*. The classical approach toward such problems in the literature, is to utilize the expectation-maximization (EM) algorithm as it has been followed in this work. In short, EM is utilized for three purposes. First, to estimate the outliers region, where no correspondence can be identified between the patient and atlas spaces, Second, to estimate the plausible regions where a partial or full correspondence between the actual patient and estimated PBMs in the atlas can be achieved, Third, to provide a framework to estimate the deformation field. In this respect, we regard the deformation field as a high-dimensional parameter set that should be estimated through EM.

This paper is organized as follows. In Section II, we briefly review our tumor generator model and introduce the relevant parameters that are estimated. In Section III, the basis of the simulation of the atlas (moving) PBMS is illustrated. The details of our EM algorithm are given in Section IV, where we derive the update equation for the deformation field. In Section VI the efficacy of this framework on both synthetic and clinical cases is evaluated, and the sensitivity of registration to the tumor parameter estimation is presented. The paper concludes in Section VII.

II. Biomechanical Tumor Modeling

The framework for modeling the glioma tumor growth and its mechanical impact on the surrounding tissue is the same as the outlined modeling by Hogea *et al.* in [20] and [35]. In this section, a brief review is given, mainly to illustrate the set of parameters that are used to simulate the tumor growth, hereafter called $\mathbf{q}$. The modeling framework consists of a reactive–advective–diffusive mass transport for tumor cells, coupled with elasticity for the brain [21], [36]. The system of PDEs governing the deformable model to simulate the glioma growth consists of

$$\begin{aligned} \frac{\partial C^{\mathbf{q}}}{\partial t} - \nabla\cdot(D\nabla C^{\mathbf{q}}) + \nabla\cdot(C^{\mathbf{q}}\mathbf{v}) - \rho C^{\mathbf{q}}(1-C^{\mathbf{q}}) &= 0 \\ \nabla\cdot[\lambda\mathbf{I}\nabla\cdot\mathbf{u} + \mu(\nabla\mathbf{u} + \nabla\mathbf{u}^T)] - f(C^{\mathbf{q}},\mathbf{p})\nabla C^{\mathbf{q}} &= 0 \\ \mathbf{v} - \frac{\partial \mathbf{u}}{\partial \mathbf{t}} &= 0 \\ \frac{\partial \mathbf{m}}{\partial t} + \nabla(\mathbf{m})\mathbf{v} &= 0 \end{aligned} \tag{1}$$

where $C^{\mathbf{q}}$, is the generated tumor density corresponding to the set of parameters $\mathbf{q}$, and $\mathbf{u}$, $\mathbf{v}$ are displacement field caused by the presence of the tumor and velocity field, respectively. The parameters include: $D \in \{D_{\mathrm{WM}}, D_{\mathrm{GM}}\}$ the diffusion coefficients, the Young modules μ, λ and proliferation coefficient ρ. Other quantities include $\mathbf{m} = (\lambda, \mu, D)$ and the $f(C^{\mathbf{q}}, \mathbf{p})$ is a function of the tumor density that controls the behavior of the mass-effect, defined as

$$f(C^{\mathbf{q}}, \mathbf{p}) = p_1 e^{(-p_2/C^{\mathbf{q}2})} e^{(-p_2/(2-C^{\mathbf{q}})^2)}. \tag{2}$$

The parameter p_2 regulates both the spatial location and the strength of the mechanical deformation caused by the tumor, while p_1 is simply a scaling factor. Given any arbitrary boundary and initial conditions over $C^{\mathbf{q}}$, $\mathbf{u}$ and $\mathbf{v}$, the system of equations in (1) are solved using a fast Eulerian continuum approach on a unmeshed grids of nodes [20]. For the set of all experiments we let zero initial conditions for the displacement and the velocity field and assume the following for the tumor density:

$$C^{\mathbf{q}}(\mathbf{x}, t=0) = \exp\left(-\frac{(\mathbf{x}-\mathbf{x_0})^2}{d^2}\right). \tag{3}$$

Where we chose d to be the same as the image resolution to allow the initial distribution to be fairly localized at $\mathbf{x}_0$. Given this definition, the set of (tumor) parameters which are estimated within our algorithm consist of

$$\mathbf{q} = \{\mathbf{x}_0, D_{\mathrm{WM}}, D_{\mathrm{GM}}, \rho, p_1, p_2\}. \tag{4}$$

III. Method

In this section, the basis of our algorithm is illustrated. We emphasize that throughout the paper we will refer to the fixed space as the patient space and the moving (warped) space as the atlas, in other words we warp the atlas to the patient space.

A. Computing Fixed Feature Images Using SVM

One of the basic challenges for intensity based tumorous image registration task, is that the relation between the observed image intensity and the density of cancerous cells, is either unknown or very complex. For example, as seen in Fig. 1, in the T1 weighted modality edema and non enhancing tumor areas have very close range of intensity values to gray matter, however the corresponding FLAIR image, reveals the edema in much better way by a hyper-intense signal around the tumor. Therefore, image intensity does not seem to be a reliable source of information for our registration task.

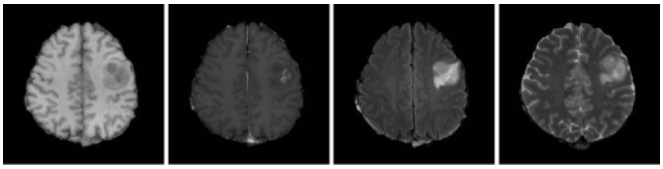

Fig. 1. Imaging profile of a glioma; from left to right: T1, Contrast enhanced T1, FLAIR and T2 images.

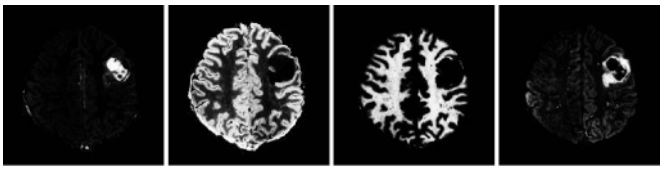

Fig. 2. Sample PBMs computed from SVM; from left to right: F_1 (tumor), F_3 (gray matter), F_4 (white matter), and F_5 (edema).

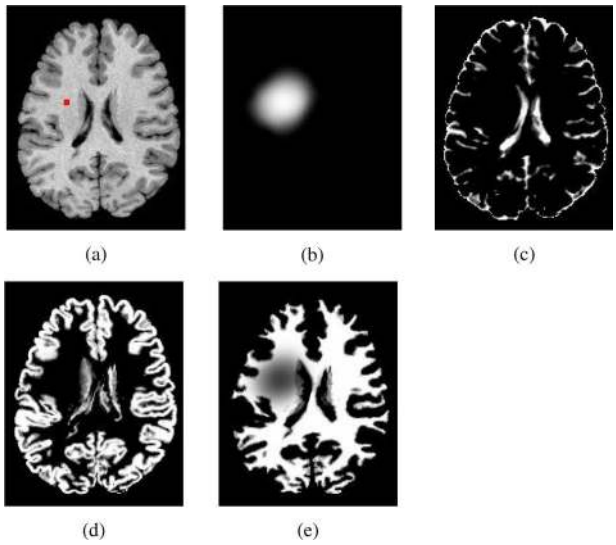

Fig. 3. Constructing the set of moving feature images. (a) T1 healthy template image segmented by FAST [37] to make original template tissue probability maps (not indicated), the marker indicates a tentative seed location designated to create moving PBMs: (b) created tumor density map $M_1^{\mathbf{q}}$; (c)–(e) $M_2^{\mathbf{q}}$, $M_3^{\mathbf{q}}$, and $M_4^{\mathbf{q}}$: tissue probability maps with mass-effect and soft-masking by tumor density map in (b), see the set of equations in (5).

As discussed in [33] multimodality imaging can help differentiating various tissue types in patients with brain tumors. Based on multiparametric imaging techniques, in [33] supervised classification using SVM was performed to segment the brain images into six different classes, namely: white matter (WM), gray matter (GM) and CSF, enhancing tumor (ET), nonenhancing tumor (NET), edema or swelling around the tumor (ED). (Necrosis was manually segmented as tumor.) In this paper a similar SVM segmentation framework has been utilized for classification of the pathological images. More specifically, we use four modalities, namely T1/T2/FLAIR and T1-CE (constrast-enhanced perfusion), as the multichannel imaging profile of the patient, and train a SVM model to compute the posterior probability maps [38] of different tissue types in the patient space. Sample results of such computed PBMs are given in Fig. 2. In the next step, these PBMs are registered to their corresponding estimated pairs in the atlas. The estimated PBMs of diseased tissue types in the atlas (moving template) are constructed using the estimated tumor density map and mass-effect. This step has been explained in further detail in Section III-B.

For simplicity, we assume that the ET and NET classes can be integrated under a unique tumor label (TU). In addition, since the necrosis is in fact the death of the cancerous cells as a result of too much density and the lack of enough nutrition, we regard it as a part of TU with probability of one, and the computed PBMs from SVM are masked to take this effect. Therefore, we can hypothesize that a set of $L = 5$ feature images $F_j(\mathbf{x})$, corresponding to different tissue PBMs computed by SVM, is defined in a fixed space Ω_F and $x \in \Omega_F$ whereas $1 \leq j \leq L$ enumerates the set of class labels: $\{\mathrm{TU}, \mathrm{CSF}, \mathrm{GM}, \mathrm{WM}, \mathrm{ED}\}$.

B. Constructing Moving Feature Images

As explained in the previous sections, diffusion-reaction equation is used for tumor growth modeling. However, edema is not modeled explicitly as this would entail complex poroelastic material [39]. Because of missing the edema in atlas, only four feature images $M_j^{\mathbf{q}}(\mathbf{x})$ corresponding to the probability maps of $\{\mathrm{TU}, \mathrm{CSF}, \mathrm{GM}, \mathrm{WM}\}$, are computed in the moving space Ω_M. Since the tumor density is in fact the partial volume of the space that has been occupied by the tumor, deterministic relations between the original PBMs of healthy moving template and those obtained after embedding the tumor can be established similar to [40]. Let a tumor density map $0 \leq C^{\mathbf{q}}(\mathbf{x}) \leq 1$ be defined in the moving space Ω_M. Such relations can be written as[1]

$$\begin{aligned} M_1^{\mathbf{q}}(\mathbf{x}) &= C^{\mathbf{q}}(\mathbf{x}) \\ M_2^{\mathbf{q}}(\mathbf{x}) &= P_{\mathrm{CSF}}(\mathbf{u}(\mathbf{x}))(1 - C^{\mathbf{q}}(\mathbf{x})) \\ M_3^{\mathbf{q}}(\mathbf{x}) &= P_{\mathrm{GM}}(\mathbf{u}(\mathbf{x}))(1 - C^{\mathbf{q}}(\mathbf{x})) \\ M_4^{\mathbf{q}}(\mathbf{x}) &= P_{\mathrm{WM}}(\mathbf{u}(\mathbf{x}))(1 - C^{\mathbf{q}}(\mathbf{x})) \end{aligned} \tag{5}$$

where $\mathbf{u}(\mathbf{x})$ is a mapping from Ω_M to Ω_M and explains the mass-effect of the tumor, and $P_l(\cdot), l \in \{\mathrm{CSF}, \mathrm{GM}, \mathrm{WM}\}$ denotes the tissue PBMs that represent the atlas structure prior to tumor growth. Note that we have $\sum_j M_j^{\mathbf{q}}(\mathbf{x}) = 1$ as they indicate modified probability maps. A sample output of (5) has been depicted in Fig. 3 that illustrates how moving side feature images, i.e., $M_j^{\mathbf{q}}(\mathbf{x})$s are produced.

IV. EM Algorithm Within the Registration Framework

As stated in Section I, our alternating framework for registration and estimation of the tumor parameters has been motivated by the EM algorithm. The cost function of our registration algorithm can be intuitively interpreted as a conditional $l2$ similarity measure between corresponding estimated moving (atlas) and real patient PBMs. However, the lack of edema information by tumor modeling in the atlas, prevents such a naive similarity to be a confident measure throughout the entire image domains. In fact, since edema is confined to white matter [40] and remains unobserved, the estimated white matter probability $M_4^{\mathbf{q}}(\mathbf{x})$

[1]In a discrete analogy, equations in (5) can be explained using expectations in multivariate hypergeometric distribution. For the sake of brevity the final equations are mentioned here.

Algorithm 1 Estimation of the optimum deformation field and tumor parameters: (Φ_o, q_o)

1: $E_{\min} \leftarrow +\infty$
2: **while** APPSPACK queue is not empty **do**
3: Pop a $\mathbf{q}$ from queue.
4: Using EM Compute: $\Phi_t = \underset{\Phi}{\operatorname{argmin}} -logf(\mathbf{Y^q}|\Phi)$.
5: $E_t \leftarrow -logf(\mathbf{Y^q}|\Phi_t)$
6: **if** $E_t < E_{\min}$ **then**
7: $E_{\min} \leftarrow E_t$.
8: $\Phi_o \leftarrow \Phi_t$.
9: $\mathbf{q}_o \leftarrow \mathbf{q}$.
10: **end if**
11: Return E_t to APPSPACK.
12: **end while**

around the tumor is not reliable. The remedy taken in this paper, is to use EM algorithm explained in Section IV-A to segment Ω_F in two different regions: a sub-domain D_0 in Ω_F within which a full vectorial $l2$ similarity measure between $M_j^{\mathbf{q}}(\mathbf{x})$ and $F_j(\mathbf{x}), 1 \leq j \leq 4$ is plausible, and D_1 in which the white matter information is excluded from driving the registration. This partitioning is guided by the patient edema's PBM, and is statistically estimated through the E step as illustrated in Section V.

A. Problem Definition and the Cost Function

Let $1 \leq i \leq N$ represent the index of an arbitrary voxel $\mathbf{x}_i$ in Ω_F and $\mathbf{h}(\mathbf{x})$ define the transformation from space Ω_F to Ω_M. Let a set of N i.i.d observation vectors be defined as

$$\mathbf{Y^q} = \Big\{\mathbf{y_i^q} | \mathbf{y_i^q} = \Big[F_1(\mathbf{x}_i) - M_1^{\mathbf{q}} \circ \mathbf{h}(\mathbf{x}_i), \ldots, F_4(\mathbf{x}_i) - M_4^{\mathbf{q}} \circ \mathbf{h}(\mathbf{x}_i)\Big]^t, \mathbf{x}_i \in \Omega_F\Big\}. \quad (6)$$

As explained in Section IV, we consider partitioning of Ω_F into D_0 and D_1. To that end we assume that the pdf of i th observation vector $\mathbf{y_i^q}$, can be modeled as a mixture of the two pdfs (f_0, and f_1) and estimate the weights of the mixture in the E step. We define f_0, and f_1 as

$$f_0\left(\mathbf{y_i^q}|\Phi\right) = \prod_{j=1}^{4} \frac{1}{\sqrt{(2\pi)\sigma_j^2}} \exp\left[-\frac{(F_j(\mathbf{x}_i) - M_j^{\mathbf{q}} \circ \mathbf{h}(\mathbf{x}_i))^2}{2\sigma_j^2}\right]$$
$$f_1(\mathbf{y_i^q}|\Phi) = \frac{1}{2} \prod_{j=1}^{3} \frac{1}{\sqrt{(2\pi)\sigma_j^2}} \exp\left[-\frac{(F_j(\mathbf{x}_i) - M_j^{\mathbf{q}} \circ \mathbf{h}(\mathbf{x}_i))^2}{2\sigma_j^2}\right] \quad (7)$$

where $\Phi = \{\mathbf{h}(\mathbf{x}_i), \sigma_1, \ldots, \sigma_4 | \mathbf{x}_i \in \Omega_F, 1 \leq i \leq N\}$ is the set of unknown parameters to be estimated. Note that the last channel information in f_1 has been replaced by a uniform distribution,[2], posing no similarity constraint on white matter.

In order to make a more compact notation in the next steps, we introduce variance matrices $\mathbf{S}_0^{-1}$, $\mathbf{S}_1^{-1}$ defined as

$$\mathbf{S}_0^{-1} = \operatorname{diag}\left(\sigma_1^{-2}, \sigma_2^{-2}, \sigma_3^{-2}, \sigma_4^{-2}\right)$$
$$\mathbf{S}_1^{-1} = \operatorname{diag}\left(\sigma_1^{-2}, \sigma_2^{-2}, \sigma_3^{-2}, 0\right). \quad (8)$$

Using these definitions equations in (7) can be written as

$$f_0\left(\mathbf{y_i^q}|\Phi\right) = \frac{1}{\sqrt{(2\pi)^4|\mathbf{S_0}|}} \exp\left[-\frac{1}{2}\left(\mathbf{y_i^q}\right)^t \mathbf{S}_0^{-1}\mathbf{y_i^q}\right]$$
$$f_1\left(\mathbf{y_i^q}|\Phi\right) = \frac{0.5\sigma_4}{\sqrt{(2\pi)^3|\mathbf{S_0}|}} \exp\left[-\frac{1}{2}\left(\mathbf{y_i^q}\right)^t \mathbf{S}_1^{-1}\mathbf{y_i^q}\right]. \quad (9)$$

Our problem of joint registration and estimation of the $\mathbf{q}$ (tumor parameters) can be defined as the optimum solution of the following problem:

$$(\Phi_o, q_o) = \underset{\Phi, \mathbf{q}}{\operatorname{argmin}} \quad -\log f(\mathbf{Y^q}|\Phi) \quad (10)$$

and

$$f(\mathbf{Y^q}|\Phi) = \prod_{i=1}^{N} \left(\sum_{k=0}^{1} \pi_k(\mathbf{x}_i) f_k\left(\mathbf{y_i^q}|\Phi\right)\right) \quad (11)$$

where $\pi_k(\mathbf{x}_i)$ is the value of the prior probability of class k at voxel $\mathbf{x}_i \in \Omega_F$. In the literature, this is achieved by applying the classical principle of the EM algorithm, minimizing an upper bound of the right hand side of (10). This requires the derivatives of the cost function with respect to the set of unknown parameters to be computed first. However, we have no analytical expression for the derivatives with respect to $\mathbf{q}$ and the numerical computation of those derivatives and following a line search algorithm to minimize the cost, can be extremely expensive in terms of CPU cycles. As a remedy we only estimate Φ within the classical EM algorithm and optimize $\mathbf{q}$ by APPSPACK, a derivative-free parallel pattern search algorithm [41]. In other words, in stead of solving (10), we decouple the minimization and solve the following problem:

$$(\Phi_o, q_o) = \underset{q}{\operatorname{argmin}}\{\underset{\Phi}{\operatorname{argmin}} -logf\left(\mathbf{Y^q}|\Phi\right)\}. \quad (12)$$

Where inner minimization with respect to Φ is achieved by EM, and outer minimization is done by APPSPACK. In practice this means that, the tumor parameters $\mathbf{q}$ are not updated through the consecutive iterations of E and M steps until convergence where the computed cost value is returned to APPSPACK as a new sample of the cost function. The computed cost value is then utilized by a search algorithm implemented in APPSPACK to inquire another sample of the cost function and identify a new minimum. Since this procedure requires several evaluations of the cost function, multiple instances of EM algorithms with different tumor parameters need to be executed. To that end, we use APPSPACK which allows us to gain a significant efficiency,

[2]Given the fact that F_j and $M_j^{\mathbf{q}}$ are probability maps staying between 0 to 1, $F_4 - M_4^{\mathbf{q}} \circ \mathbf{h}$ is a random variable between $[-1, 1]$ hence the corresponding uniform distribution is 0.5.

thanks to its parallel execution. The procedure has been illustrated through the algorithm 1.

The parameter estimation can be made robust by modeling the "outliers" class. This is particularly important in our registration application, since it allows relaxation of the similarity constraint whenever no actual correspondence can be established between the patient and atlas images. To that end, the ML cost in (10) is modified by implicitly introducing a third rejection class. Similar to segmentation framework outlined in [42], at every iteration: m, given the current estimate of the unknown parameters $\Phi^{(m-1)}$, the modified likelihood for parameter estimation is written as

$$Q^{\mathbf{q}}(\Phi|\Phi^{(m-1)}) = \sum_{i=1}^{N}\sum_{k=0}^{1} p_{ik}^{(m)} log\left(f_k\left(\mathbf{y_i^q}|\Phi\right) + \lambda\right). \quad (13)$$

In which λ is a small constant. Increasing λ also increases the robustness on the parameter estimation (registration), but also adversely affects the sensitivity with respect to segmentations. In this paper, we found $\lambda \simeq 1e^{-3}$ to be a good compromise between robustness and sensitivity. $p_{ik}^{(m)}$ stands for posterior probability at iteration m of class k at voxel i, computed in E step as[3]

$$p_{ik}^{(m)} = \frac{f_k\left(\mathbf{y_i^q}|\Phi^{(m-1)}\right)\pi_k(\mathbf{x}_i)}{\Sigma_l f_l(\mathbf{y_i^q}|\Phi^{(m-1)})\pi_l(\mathbf{x}_i)}. \quad (14)$$

We use the edema's PBM measured by our SVM classifier in the previous section for setting: $\pi_0(\cdot) = 1 - F_5(\cdot)$ and $\pi_1(\cdot) = F_5(\cdot)$. As explained in [42], robust estimation of Φ can now be achieved by maximizing

$$Q^{\mathbf{q}}(\Phi|\Phi^{(m-1)}) = \sum_{i=1}^{N}\sum_{k=0}^{1} w_{ik}^{(m)} log\left(f_k\left(\mathbf{y_i^q}|\Phi\right)\right) \quad (15)$$

where

$$w_{ik}^{(m)} = p_{ik}^{(m)} \frac{f_k\left(\mathbf{y_i^q}|\Phi^{(m-1)}\right)}{f_k\left(\mathbf{y_i^q}|\Phi^{(m-1)}\right) + \lambda}. \quad (16)$$

The computed weights $w_{ik}^{(m)}$, $k = 0, 1$ at every voxel i define the membership values of that voxel to each cluster k. Therefore, they represent an statistical estimation for the partitioning of the Ω_F to D_0 and D_1. A couple of sample partitioning has been indicated in Fig. 4, which also illustrates that how the extracted edema's PBM from SVM, are utilized as spatial prior functions for such segmentations.

B. Estimation of ϕ

Because the number of unknown parameters to be estimated in Φ is very large ($\simeq N^3$), the estimation problem is highly ill-posed. Robust estimation could be achieved by smoothness constraint over deformation field i.e., $\mathbf{h}_i$s modeled through a Markov random field, however, such an approach makes the closed form solutions difficult. Here we choose to relax this constraint and derive an explicit form for $\mathbf{h}_i$s and then project the obtained deformation to the space of the acceptable deformations (merely smooth or diffeomorphic transformations). Therefore, although the deformation field is explicitly estimated according to maximum-likelihood principle, it is smoothed by convolution with a Gaussian filter, similar to Thirions' demons framework [43].

[3]We will refer to the iteration number in parenthesized upper indexes throughout the rest of paper. In addition vectors and matrices are notified in bold fonts.

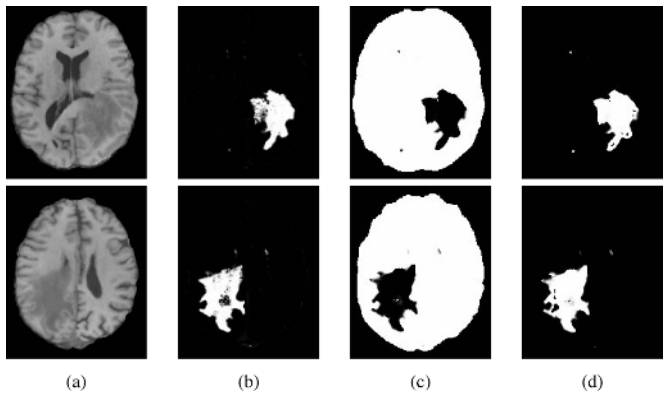

Fig. 4. Automatic partitioning of Ω_F through (16) in the E step: (a) Patient T1 image, (b) edema's probability map (F_5) measured by our SVM classifier is used as the prior map for D_1 i.e., $\pi_1(\cdot)$, (c) computed membership function for class one (w_0), and (d) computed membership function for class zero (w_1) in steady state.

In M step, in addition to updating the variances, we derive the update equation for the deformation field using directional derivative principle. To that end, the variation of (15) with respect to an infinitely small and arbitrary test function ψ, is assigned to zero, i.e.,

$$\begin{aligned}\langle \partial Q^{\mathbf{q}}(\Phi|\Phi^{(m-1)}), \boldsymbol{\psi}\rangle &= \lim_{||\psi||\to 0}\Big\{Q^{\mathbf{q}}(\Phi^{(m-1)} + \boldsymbol{\psi}|\Phi^{(m-1)}) \\ &\qquad - Q^{\mathbf{q}}(\Phi^{(m-1)}|\Phi^{(m-1)})\Big\} \\ &= 0 \end{aligned} \quad (17)$$

where $\Phi^{(m-1)} + \boldsymbol{\psi} = \{\mathbf{h}^{(m-1)}(\mathbf{x}_i) + \mathbf{v}(\mathbf{x}_i)|\mathbf{x}_i \in \Omega_F, 1 \le i \le N, \sigma_j^{(m-1)} + \varepsilon_j, 1 \le j \le 4\}$. Replacing (7) in (15) and keeping the second-order terms, as the proof is given in the appendix, the update rule of the velocity field can be obtained by the solution to the following $1 \le i \le N$ independent linear systems:

$$\mathbf{W}_i^{(m-1)}.\mathbf{v}_i = -\mathbf{r}_i^{(m-1)} \quad (18)$$

where matrix $\mathbf{W}_i$ is defined as

$$\begin{aligned}\mathbf{W}_i^{(m-1)} = \nabla\mathbf{M} \circ \mathbf{h}_i^{(m-1)}\Big[&w_{i0}^{(m-1)}(\mathbf{S_0}^{(m-1)})^{-1} \\ &+ w_{i1}^{(m-1)}(\mathbf{S_1}^{(m-1)})^{-1}\Big]\left(\nabla\mathbf{M} \circ \mathbf{h}_i^{(m-1)}\right)^t \end{aligned} \quad (19)$$

$\nabla\mathbf{M}$ is a 3×4 matrix defined by column-wise concatenating of the gradient vectors of the moving PBMs, i.e.,

$$\nabla\mathbf{M} = [\nabla M_1^{\mathbf{q}} \quad \nabla M_2^{\mathbf{q}} \quad \nabla M_3^{\mathbf{q}} \quad \nabla M_4^{\mathbf{q}}] \quad (20)$$

$\mathbf{r}_i^{(m-1)}$ is defined as

$$\begin{aligned}\mathbf{r}_i^{(m-1)} = 2\Big[&w_{i0}^{(m-1)}\left(\mathbf{S_0}^{(m-1)}\right)^{-1} \\ &+ w_{i1}^{(m-1)}\left(\mathbf{S_1}^{(m-1)}\right)^{-1}\Big]\mathbf{y_i^{q(m-1)}}. \end{aligned} \quad (21)$$

Solution to (18), similar to [43], can be made more stable by adding a norm penalizing term for the update velocity $\mathbf{v}_i$ at the left-hand side

$$\left[\mathbf{W}_i^{(m-1)} + \frac{\mathbf{I}_{3\times 3}}{\left(\delta_i^{(m-1)}\right)^2}\right]\mathbf{v}_i = -\mathbf{r}_i^{(m-1)} \tag{22}$$

where $(\delta_i^{(m-1)})^2$ is proportional to the maximum norm of the update ($\|\mathbf{v}_i\|$). In this paper we define it as

$$\left(\delta_i^{(m-1)}\right)^{-2} = \frac{\left(y_{i1}^{\mathbf{q}}\right)^2}{\left(\sigma_1^{(m-1)}\right)^2} + \sum_{j=2}^{4}\left(y_{ij}^{\mathbf{q}}\right)^2 \tag{23}$$

where $y_{ij}^{\mathbf{q}}$ denotes the jth element of the vector $\mathbf{y}_i^{\mathbf{q}}$. The reason for such selection is empirical and can be explained as follows: because of the initial approximate alignment, the variances are in practice much smaller than one, i.e., $\sigma_j^{(m-1)} \ll 1$. Therefore in the regions far separated from the tumor where $(y_{i1}^{\mathbf{q}})^2 \approx 0$, the registration is dominated by $\mathbf{W}_i^{(m-1)}$, whereas in regions where $\sigma_1^{(m-1)} \ll (y_{i1}^{\mathbf{q}})^2$ i.e., adjacent to tumor, $\left(\delta_i^{(m-1)}\right)^{-2}$ takes large values and therefore the norm of the update vector $\|\mathbf{v}_i\|$ is further penalized. This property is important and minimizes unrealistic warping in the vicinity of tumors.

Another distinction of our formulation from the original demons algorithm presented in [43] and [44], is the mechanism for estimation and masking out the outliers by the engagement of the time varying weights in the update (22). In fact, it is easy to see that for any outliers making $w_{i0}^{(m-1)} \approx 0$ and $w_{i1}^{(m-1)} \approx 0$, the update vector $\mathbf{v}_i$ will be very small, and therefore its contribution in the subsequent smoothing step is minimized. Update equations for the variances, σ_j, $1 \le j \le 3$, with similar principle to [42] can also be derived as

$$\sigma_j^{(m-1)} = \frac{\sum_{i=1}^{N}\left(w_{i0}^{(m-1)} + w_{i1}^{(m-1)}\right)y_{ij}^2}{\sum_{i=1}^{N}\left(w_{i0}^{(m-1)} + w_{i1}^{(m-1)}\right)} \tag{24}$$

and

$$\sigma_4^{(m-1)} = \frac{\sum_{i=1}^{N} w_{i0}^{(m-1)} y_{i4}^2}{\sum_{i=1}^{N} w_{i0}^{(m-1)}}. \tag{25}$$

From these equations, $\left(\mathbf{S}_0^{(m-1)}\right)^{-1}$, $\left(\mathbf{S}_1^{(m-1)}\right)^{-1}$ are constructed in accordance with the definitions in (8). In order to obtain the updated deformation field, we solve (22) and set[4]:

$$\mathbf{h}_i^{(m)} = \mathbf{h}_i^{(m-1)} - \left[\mathbf{W}_i^{(m-1)} + \frac{\mathbf{I}_{3\times 3}}{\left(\delta_i^{(m-1)}\right)^2}\right]^{-1}\mathbf{r}_i^{(m-1)} \tag{26}$$

[4]In fact, we follow [43], [44] and in stead of addition, a composition update rule is used i.e., $\mathbf{h}_i^{(m)} = \mathbf{h}_i^{(m-1)} \circ \mathbf{v}_i$, to achieve a faster convergence.

C. Estimation of $\mathbf{q}$

Simultaneous estimation of the warping and tumor parameters is a highly ill-posed problem. In order to make a better estimation of $\mathbf{q}$, we propose to constraint the solutions in such a way that the estimated tumor densities have the same mass (expected probability) as the target real tumor in the patient image. In particular given a target tumor PBM in the fixed domain $P_{\mathrm{TU}}(\mathbf{x})$, the following constraint is desired

$$\int_{D_F} P_{\mathrm{TU}}(\mathbf{x})dx \approx \int_{D_M} C^{\mathbf{q}}(\mathbf{x})dx. \tag{27}$$

The approximation is because we are only able to carry out the forward tumor simulation, and no target tumor mass can be accurately specified before hand.[5] The tumor growth is pursued until the total mass of the created tumor density exceeds the target mass minimally. The difference between target and created mass values on atlas, depends on the size of time step of the forward simulation process and in order to minimize it smaller time steps are desired. In practice we observed that choosing the time step of five days, is sufficiently small to keep this error within the five percent of the target mass.

V. Implementation Details

For every patient, our preprocessing pipeline starts with skull stripping and cerebellum removal of all modalities (T1/T2/FLAIR/T1-CE). Next, these images are co-registered using the FLIRT algorithm [45] to construct the set of the voxel-wise feature vectors required by SVM classifier. In order to train our SVM classifer, an expert radiologist in our center was requested to delineate some representative regions of the different tissue types for a couple of sample data sets as described in Section III-A. Using these ROIs, a nonlinear Gaussian kernel based SVM model is trained according to principles illustrated in [38]. For the subsequent test subjects, before application of the SVM, all modalities are histogram matched to their corresponding modalities in the training samples.

Prior to application of our deformable registration, the computed PBMs of each patient and the atlas should be linearly registered. Our atlas has the same image dimension of $256 \times 256 \times 128$ and voxel size of $0.9375 \times 0.9375 \times 1.5$ mm^3 as utilized in [20]. In order to keep the consistency with this optimal lattice specifications, we linearly register the computed PBMS to our atlas using FLIRT. The affine transformed PBMs obtained in this way, are then utilized as the fixed reference feature images.

Our deformable registration approach, is implemented using a multiscale framework. In order to minimize the risk of convergence to local optimums, registration starts with lower resolutions and the computed deformation field after interpolation is set as the initial field in the next level. A down sampling pattern of 4:2:1 is used to construct the three-level pyramids of both the estimated and patient PBMs.

[5]Another alternative would be to introduce a "soft constraint" as *a prior* information term to penalize the difference between the mass values. However, that would have required a weighting parameter to be selected by user, therefore it was avoided here.

In order to make faster tumor simulations, the set of equations in (1) is solved on a lattice of $65 \times 65 \times 65$ nodes, down-sampled from the original atlas space [20]. The estimated tumor density is then up-sampled to create the diseased PBMs using the equations in (5). In order to find the best tumor simulation parameters, the APPSPACK optimization library launches several parallel MPI registration jobs assigned with different set of tumor parameters on a Linux cluster with Dual Intel Xeon 2.80 GHz CPUs. Each process returns the registration cost value to APPSPACK until there is no other point left in the queue as specified in Algorithm 1. Furthermore, in order to reduce the computation burden this procedure is only executed in the coarsest level of the pyramids and for a few (ten) iterations. After estimation of the best $\mathbf{q}$, the registration is iterated with the finest resolution and more number of iterations.

The initial seed location was set as the center of the search span which is defined by the user. Affine registered patient image to atlas, was utilized to evaluate the extent of the tumor. We observed that the span of $4 \times 4 \times 4$ cm^3, was sufficiently large to cover the major parts of the tumorous bulks and to ensure that the estimated seed will be located inside of the search span. In addition, the following search span was utilized for the rest of other parameters whenever not mentioned: $0.01 \leq \rho \leq 0.1$, $0.01 \leq p_1 \leq 12$, $0 \leq p_2 \leq 0.02$, and $1e^{-13} \leq D_g, D_w \leq 1e^{-7}$.

Registration module has been coded in C++ using *Insight Toolkit* library, and the template class was based on the contributed code of Vercauteren *et al.* [44]. Inherited properties from this object oriented programming, allows us to enforce different constraints on the deformation field such as diffeomorphism (compositive update rule), simple smoothness (additive update rule), linear elasticity and viscosity. In this work we have been using diffeomorphic transformation model, and in each iteration the computed deformation is smoothed with a Gaussian kernel of $\sigma = 2$. This value is kept fixed during all of our experiments.

VI. Results

The registration accuracy is evaluated on both simulated and real PBMs of glioma. The simulated PBMs are produced by embedding a tumor on a synthetic brain image [shown in Fig. 5(a)] made by deforming our standard atlas [shown in Fig. 3(a)]. The deformation field was exactly known and was generated by statistically simulated deformations (SSD) introduced in [46]. The same standard atlas of Fig. 3(a) was then registered to simulated patient PBMs, and the estimated deformation field was compared to the ground truth which was available to us using SSD.

To assess the registration performance of our real glioma images, we use the same subject independent evaluation method utilized in [47]. In particular we measure Jaccard ratios to evaluate the overlap between the warped labels from atlas, and the reference labels obtained from our SVM classifier. This is because, in general we found the glioma images to be extremely complex (especially around the tumor) to allow finding exact correspondences between the patient image and the atlas. Therefore the evaluation method utilized in [18] was not reliable in this study.

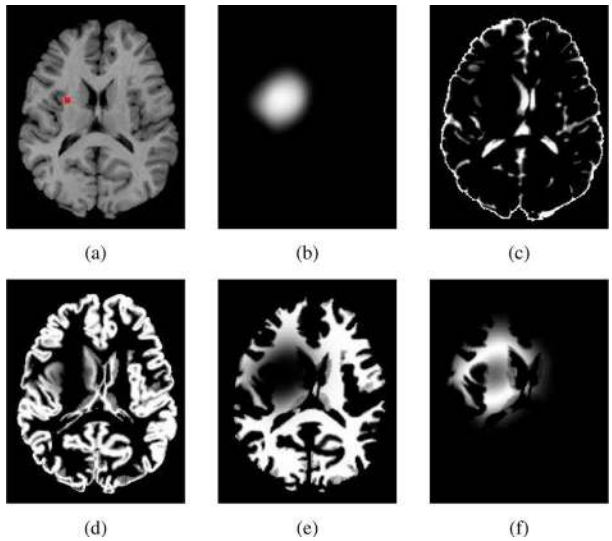

Fig. 5. Using statistically simulated deformations (SSD) to create reference feature images (PBMs). (a) Sample generated T1 image by SSD using Fig. 3(a) as the base template, the marker indicates the seed location designated to create reference (fixed) PBMs: (b) created tumor density map F_1; (c)–(e) F_2, F_3, and F_4: tissue probability maps with mass-effect and soft-masking by the created tumor density map in (b), (f) simulated edema F_5 using (28).

A. Simulating Reference PBMs for Validation Purpose

For the purpose of measuring the registration accuracy using SSD, reference (fixed) PBMs should be simulated. In a real patient case, these are supplied through our SVM classifier as shown in Fig. 2. The difficulty arisen in simulating these PBMs is because of the fact that we do not create edema through application of our biophysical tumor model, whereas in real images, edema is present. To fill out this gap we propose an *ad hoc* formulation for edema, we emphasize that this is only meant for data simulation for validation purposes and the registration algorithm itself is independent of this formulation.

Edema simulation is based on the observation that the probability of finding the edema is maximized somewhere in between the tumor bulk (i.e., $C^{\mathbf{q}} = 1.0$) and the healthy tissue (i.e., $C^{\mathbf{q}} = 0.0$). Therefore the simulated PBM of edema is proposed to be in the form of $C^{\mathbf{q}}(1 - C^{\mathbf{q}})$, which has the maximum on $C^{\mathbf{q}} = 0.5$. We also assume that the edema should be confined into white matter. Given these intuitions, the proposed set of equations to simulate our reference PBMs for validation experiments is very similar to (5) but includes the edema's PBM

$$\begin{aligned}
F_{\mathrm{sim}_0}(\mathbf{x}) &= C^{\mathbf{q_0}}(\mathbf{x}) \\
F_{\mathrm{sim}_1}(\mathbf{x}) &= P_{\mathrm{CSF}}(\mathbf{h}_{\mathrm{ssd}} \circ \mathbf{u}(\mathbf{x}))(1 - C^{\mathbf{q_0}}(\mathbf{x})) \\
F_{\mathrm{sim}_2}(\mathbf{x}) &= P_{\mathrm{GM}}(\mathbf{h}_{\mathrm{ssd}} \circ \mathbf{u}(\mathbf{x}))(1 - C^{\mathbf{q_0}}(\mathbf{x})) \\
F_{\mathrm{sim}_3}(\mathbf{x}) &= P_{\mathrm{WM}}(\mathbf{h}_{\mathrm{ssd}} \circ \mathbf{u}(\mathbf{x}))(1 - C^{\mathbf{q_0}}(\mathbf{x}) - C^{\mathbf{q_0}}(1 - C^{\mathbf{q_0}})) \\
F_{\mathrm{sim}_4}(\mathbf{x}) &= P_{\mathrm{WM}}(\mathbf{h}_{\mathrm{ssd}} \circ \mathbf{u}(\mathbf{x}))(C^{\mathbf{q_0}}(1 - C^{\mathbf{q_0}}))
\end{aligned} \tag{28}$$

where F_{sim_4} stands for edema's PBM, $\mathbf{u} : \Omega_F \rightarrow \Omega_F$ is the mass-effect deformation estimated by our tumor generator model [20], q_0 is the tumor parameter set used to create the tumor density map $C^{\mathbf{q_0}}$ and $\mathbf{u}$, and $\mathbf{h}_{\mathrm{ssd}} : \Omega_F \rightarrow \Omega_M$ is the statistically simulated deformation learned from a bank of

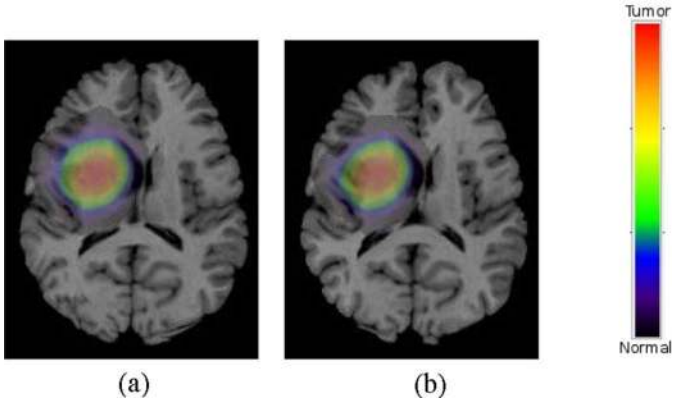

Fig. 6. Registration results using simulated patient PBMs; Left: The patient T1 image corresponding to the target PBMs shown in Fig. 5(b)–(f) overlayed by the target tumor density, Right: registered atlas overlayed by the warped tumor density.

normal-to-normal warping sets [46]. Note that these PBMs sum up to one, as required for an actual set of tissue probability maps in a real patient. We use FAST [37], to segment a T1 template atlas image given in Ω_M, into three different labels, and compute the posterior probability map for each tissue label, i.e., $P_{\rm CSF}$, $P_{\rm GM}$, and $P_{\rm WM}$. The computed tissue maps are then plugged in (28) to hand in the simulated reference PBMs. As seen in (28), the data in atlas ($P_{\rm CSF}$, $P_{\rm GM}$, and $P_{\rm WM}$) is linked to the reference feature images, by the compositive mapping of $\mathbf{h}_{\rm ssd} \circ \mathbf{u}(\mathbf{x})$. Because both the mass effect $\mathbf{u}$ and $\mathbf{h}_{\rm ssd}$ are computed, the ground truth for the total deformation field is known and can be used for validation purposes. A sample set of the constructed PBMs using (28) has been given in Fig. 5.

B. Evaluation Using Simulated PBMs By SSD

We simulated five sets of reference PBMs and evaluated both registration accuracy and estimated tumor parameters in accordance with principles illustrated in Section VI-A. Different seed locations with various diffusion coefficients were utilized to created these reference PBMs. As a result, they were different in both tumor locations and diffusion patterns. It should be emphasized that the same template used by SSD to create the reference PBMs in (28), is utilized to create moving PBMs as illustrated in Section III-B. Estimation of the best tumor parameter set and deformation field is achieved using the procedure in Algorithm 1 and the principles illustrated in Section IV-B. A sample registration result is shown Fig. 6, in which the target T1 image is made by warping the template image in Fig. 3(a) through $\mathbf{h}_{\rm ssd} \circ \mathbf{u}(\mathbf{x})$. The result shows a good match between the target and warped images and tumor densities. The color bar aside indicates the region covered by red color is fully replaced by the tumor, while the rest of spectrum is used to indicate diffusion and infiltration.

The five sets of tumor parameters used to create the synthetic reference PBMs, have been summarized in Table I. Each row corresponds to one experiment specified by a unique $\mathbf{q_0}$ in (28). In these experiments, we chose $p_1 = 0$ and $\rho = 0.025$ during both simulation of reference PBMs and registration. This setting corresponds to have $\mathbf{u}(\mathbf{x}) = \mathbf{x}$. Therefore the registration accuracy can be directly computed by comparing the estimated deformation field to the SSD created deformation, i.e., $\mathbf{h}_{\rm ssd}$. Table II summarizes the estimated tumor parameters. It shows that the tumor seeds in patient and the atlas are registered with high spatial accuracy, since the estimated seed locations in atlas are mapped very closely to the patient's tumor seed locations. (To see this compare the x_c, y_c, z_c in corresponding rows in Table I). However, the estimated diffusion coefficients are different from the values in Table I utilized to simulate the reference patient PBMs. This is because, the tumor growth PDE model in (1) has been solved in different domains (patient versus atlas), which have different portions of GM, WM, and CSF. Therefore it is not possible to estimate the same diffusion parameters. Registration accuracy in terms of root-mean-square error, has been summarized in Table III. As shown, the rms errors are evaluated on three zones. These regions are delineated by thresholding the reference tumor density map, i.e., C_{q_0}, in two different levels, leaving the entire image domain into far, intermediate and near zones (with respect to tumor location). For example, the third column corresponds to rms registration error on and in the vicinity of the tumor, where the tumor density is high. The last row is the column wise average of reported errors. As seen, the average rms registration error on the far zone (healthy areas) is comparable to the diagonal size of the image voxels (2.1 mm), and deteriorates on the intermediate and near zones (with no significant differences on the averages). The the maximum rms of (3.25 mm) can be found in the near zone, and falls within the diagonal size of the voxel size used for tumor simulation (4.8 mm). It should be pointed out that we do not compare our method to ORBIT using the images created

TABLE I
COORDINATES OF THE TUMOR CENTERS (IN Ω_F) AND THE DIFFUSION COEFFICIENTS USED TO SIMULATE FIVE SETS OF REFERENCE PBMS

Set no.	x_c	y_c	z_c	d_w	d_g
1	101.493	63.4347	79.3623	1e-8	0.5e-8
2	147.798	153.792	108.928	2e-8	0.5e-8
3	101.499	116.723	107.319	1e-8	0.5e-8
4	140.288	99.9364	122.25	2e-8	0.5e-8
5	105.94	150.00	101.81	1e-8	0.5e-8

TABLE II
ESTIMATED TUMOR CENTERS (MAPPED TO Ω_F) AND DIFFUSION COEFFICIENTS OF THE FIVE SIMULATED PATIENTS PBMS CORRESPONDING TO TABLE I

Set no.	x_c	y_c	z_c	d_w	d_g
1	101.5	62.7969	79.0937	0.65e-8	.5e-8
2	148	153.906	110.0	1.4e-8	1e-8
3	101.547	116.25	107.094	0.5e-8	0.5e-8
4	139.75	100.453	122.094	2.21e-08	0.505e-8
5	105.1	149.23	100.94	1.4e-08	0.505e-8

TABLE III
REGISTRATION ACCURACY (IN MILLIMETERS) WITH RESPECT TO GROUND TRUTH DEFORMATION IN THREE DIFFERENT ZONES OF TUMOR DENSITY

	$C \leq 1e-5$	$1e-5 \leq C \leq 0.5$	$0.5 \leq C \leq 1$
1	2.49	3.1	2.18
2	2.638	3.04	3.58
3	2.67	3.14	3.08
4	2.37	3.28	3.73
5	2.5	3.18	3.63
Avg.	**2.53**	**3.14**	**3.25**

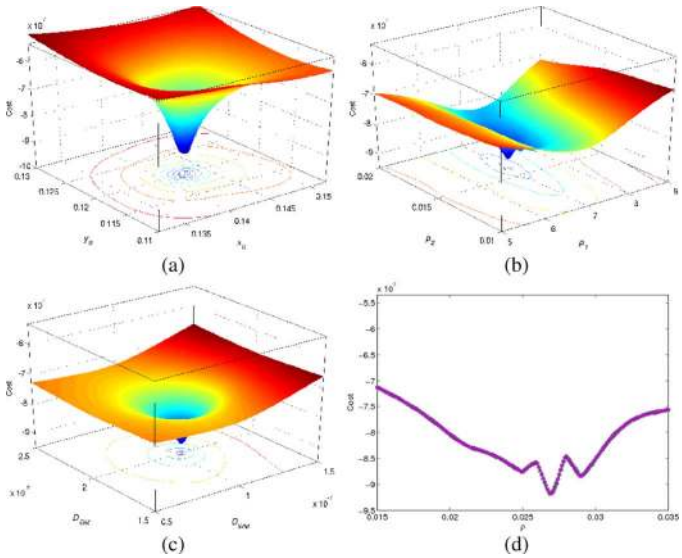

Fig. 7. Two-dimensional profiles of the cost function versus estimated tumor parameters ($\mathbf{q}$). Sensitivity across: (a) tumor seed coordinates, (b) mass-effect parameters, (c) diffusion coefficients, (d) proliferation coefficient. The estimated parameters are reasonably around the target values. The largest sensitivity is achieved versus change in the tumor seed location.

by SSD [46]. The reason is because SSD uses HAMMER [12] generated deformation fields as training samples. Those deformation fields are easily captured by ORBIT, since ORBIT has been build on the basis of HAMMER (they are basically same registration procedures on healthy parts of brain). Therefore, the simulated images are highly biased in favor of ORBIT, making such comparison not to be fair.

C. Sensitivity of the Cost Function with Respect to $\mathbf{q}$

In order to test the potential of optimizing the tumor growth parameters using the proposed optimality criterion, we have plotted the total cost as a function of the error in estimating $\mathbf{q}$. We should emphasize that for an inter-subject registration task, because the PDEs introduced in (1) should be solved in two different domains, it is not possible to estimate exactly the same tumor parameters. Therefore, the results in this section have been obtained using an intra-subject registration task. To that end, we only simulate a mass-effect on the template, i.e., we put $\mathbf{h}_{\text{ssd}}(\mathbf{x}) = \mathbf{x}$ in our estimated PBMs in (28), and try to estimate the original $\mathbf{q_0}$. The computed cost values are then interpolated within the 2-D planes intersecting the estimated $\mathbf{q}$, as shown in Fig. 7. As shown, the cost function in general remains locally convex with regard to the most of the parameters and they have been estimated reasonably around the target values (central values of the indicated ranges). As seen in panels (b) and (d), there are some fluctuations around the target values. We believe that this is because of lacking edema as a part of our estimated moving feature images, and also numerical errors arisen when the registration errors are very small. In addition, Fig. 7 indicates that the largest sensitivity is achieved versus the change in the tumor seed location, and this is followed by diffusion coefficients, mass-effect parameters and proliferation coefficient.

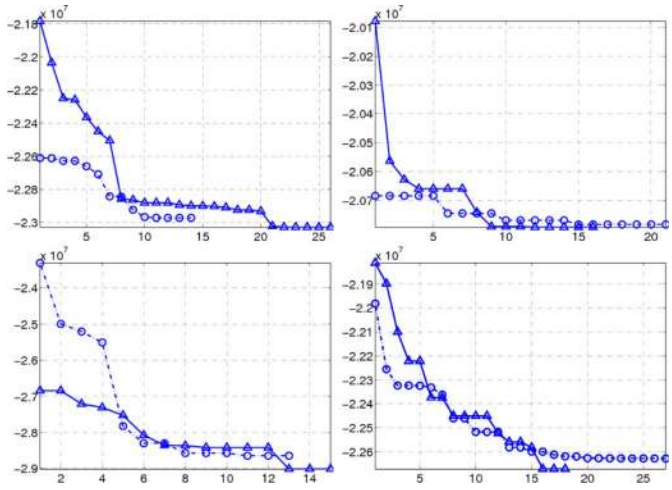

Fig. 8. Convergence plots of four real sample subjects. Vertical and horizontal axes indicate the cost value and number of minimizing registrations. Each panel corresponds to a single subject and represents the minimization of the cost function with two different search span for tumor parameters.

D. Robustness and Convergence Analysis

Because of the larger number of tumor parameters (compared to ORBIT), and the combination of two different optimization algorithms the overall robustness of the algorithm was of major interest. We evaluated the robustness and convergence behavior of the algorithm using four real glioma patients. For every individual a pair of registration experiments with different search spans of tumor parameters $\mathbf{q}$ was performed. To that end, the search span for $\mathbf{q}$ in the first experiment was enlarged by 50% in every dimension to define a new search span for the second experiment. Of especial interest was to evaluate that how the converged values of $\mathbf{q}$ are different from each other. For an ideally robust estimation with a global minimum, those values should be same. However, our experiments showed that the cost function was not convex and therefore different tumor parameters were estimated. For every individual each panel in Fig. 8 shows that how the cost values drop to different local minimums. Note that the horizontal axis counts the number of "successful" registrations in which APPSPACK have found a new minimizing value. For every patient the corresponding converged tumor parameters using different search spans of $\mathbf{q}$, have been listed in a single row of Table IV (because of moderate sensitivity on p_2, its value was fixed to zero in these experiments). The comparison of the converged tumor parameters for each patient shows that the estimated tumor center locations are minimally different compared to e.g., diffusion coefficients, and they can be estimated more robustly. For the third subject, the dimensionality of the search space was reduced by fixing the diffusion coefficients, therefore optimization was done with respect to other tumor parameters. Consequently, overall a more robust estimation was achieved on the rest of parameters.

In addition, the impact of convergence into different local minimums on the registration errors has been studied by measuring the Jaccard overlap ratios in Table V (refer to Section VI-E-I for definition and further details). The table indicates that lower cost values (E in the second column)

TABLE IV
ESTIMATED VALUES OF THE TUMOR PARAMETERS $\mathbf{q}$ CORRESPONDING TO FIG. 8 USING APPSPACK

Subj.	x_c	y_c	z_c	p_1	ρ	d_w	d_g
1	13.2	14.0	9.0	.05	6.2	6e-9	1.5e-9
	13.2	14.5	9.0	.03	7	8e-9	5.5e-9
2	11.5	10.8	8.9	.06	6	1.5e-10	5e-13
	11.3	11.4	9.4	.06	5	1.5e-11	1e-12
3	11.0	11.0	12.4	.01	5.0	1.5e-9	1e-10
	11.0	11.0	12.7	.01	7.5	1.5e-9	1e-10
4	14.3	7.2	9.8	.04	3.3	1e-7	1.5e-9
	14.3	7.2	9.8	.02	3.5	5e-8	1.0e-9

TABLE V
JACCARD RATIOS OF VARIOUS TISSUE LABELS CORRESPONDING TO CONVERGED LOCAL MINIMUMS IN FIG. 8

Subj.	$E(\times 10^7)$	L-Vent	Tum	L-GM	L-CSF
1	-2.29	54.5%	38.2%	57.19%	20.0%
	-2.30	55.1%	42.2%	56.13%	24.0%
2	-2.05	65.5%	48.6%	60.0%	20.9%
	-2.08	65.7%	47.6%	60.0%	25.2%
3	-2.86	60.0%	38.4%	49.0%	17.4%
	-2.90	61.2%	40.4%	49.7%	19.4%
4	-2.262	56.5%	68.9%	67.0%	18.5%
	-2.267	58.6%	72%	68.9%	18.9%

generally imply larger overlap ratios on various tissue labels and therefore a better registration quality.

E. Registration of Real Glioma Images

Fifteen multichannel data sets of real gliomas with different grades, and sizes were selected for registration with the normal template (atlas) and the comparison was made to ORBIT [19]. The preprocessing step and the implementation details are illustrated in Section V.

As the reference input, ORBIT requires a label image which should be created by segmentation of the patient image. For that purpose the hard segmentations (tissue labels) obtained through our SVM was used for each subject. Therefore, the advantage of using multiparametric images for segmentation has also been utilized in ORBIT. Moreover, since some of our glioma images contain large portions of edema, and the ORBIT does not handle this type of tissue label, we replace edema by WM. This is based on our hypothesis that edema only spreads into white matter. Therefore, the performance of ORBIT was increased substantially. Other details and parameters were same as in [19]. In terms of computational cost, having the tumor parameters our registration method runs faster, however since we estimate eight parameters, versus four parameters in ORBIT, the total computation cost stays similar to ORBIT and depending on the tumor size may vary between $(6 \sim 14\ \mathrm{h})$.

1) Quantitative Assessment: As illustrated in Section VI, the complexity of glioma images, especially around the tumor, makes the task of finding of corresponding landmarks between the patient image and the atlas difficult and unreliable. Therefore the evaluation method utilized in [18] was not a robust measure for this study. In this paper similar to [47], the rater independent Jaccard ratio, measuring the overlap between target (from SVM) and warped labels from atlas, has been utilized for quantitative evaluations. More specifically for each label k we measure

$$JR_k = \frac{n(T_k \cap W_k)}{n(T_k \cup W_k)} \tag{29}$$

where n represent the number of voxels in a set, T_k is the set of voxels that have been labeled as k in patient, and W_k is the set of voxels obtained by warping of voxels originally labels as k in atlas.

In order to be discriminative on performance for local (tumor vicinity) and global regions (rest of the healthy portions), the warped tumor density created in atlas space, was segmented by a threshold of $1e^{-5}$ to divide the patient image space into two separate regions denoted as local (L) and global (G). Next, the intersections of these regions with SVM segmented GM, CSF and TUM, along with manually segmented ventricles Vent were used to create different target labels. Note that the normal part of the WM (excluding edema) is not used in the quantitative evaluation. This is because we do not model edema in atlas, and WM in atlas is in fact a mixture of edema and white matter where we do not have a border to separate them.

The measured Jaccard ratios for all of our fifteen test subjects are shown using bar and scatter plots in Fig. 9. In addition a paired t-test was used to identify statistically meaningful differences between measurements. Table VI summarizes the mean JR measures made by averaging though all test subjects both for ORBIT and our method. As seen our method outperforms the ORBIT in most of the labels, by minimum margin of 6.3% on tumors and maximum 21.15% on G-CSF.

2) Qualitative Assessment: In addition to quantitative results based on the label overlaps, the registration performance of our method is also visually evaluated. The registration results of eight test subjects of different grades of glioma, with the normal atlas and its comparison to ORBIT are illustrated in Figs. 10 and 11. The normal atlas in these experiments was the same atlas in Fig. 3 used in our previous sections. From left to right, first column show the T1 images (other modalities are not shown), the second column show the PBMs (reference tissue probability maps) of tumor and gray matter, obtained through our SVM classifier. This is followed by the ORBIT and our proposed method's results. Similar color bar in Fig. 6 has been utilized to overlay the warped tumor density on the warped atlas images in our method. It is important to note that the regions overlayed by red are fully replaced by the tumor. The presence of other structures in these areas, denote how they have been captured by the tumor, and should not be taken as their real existence. This complexity in rendering the results is indispensable, because we had no clues on the change of image intensity levels by presence of tumor. Also, since ORBIT does not generate diffused tumor densities, only the estimated tumor labels are presented. Green markers in the first column indicate some locations where our method has achieved a better similarity in comparison to ORBIT.

In general, very good similarities between the warped atlas overlayed by the warped tumor densities, and the patient images can be observed for all cases using our method. Also, the warped tumor densities resemble the reference PBMs, and overall match the pathological areas.

The patients indicated in Fig. 10 have been diagnosed with various grades of gliomas and the tumors with infiltration. In the first sample ORBIT has captured the infiltrated tumor parts as a bulk mass, and some unrealistic mass-effect has been generated [top rows in (c)]. Whereas the warped tumor density using

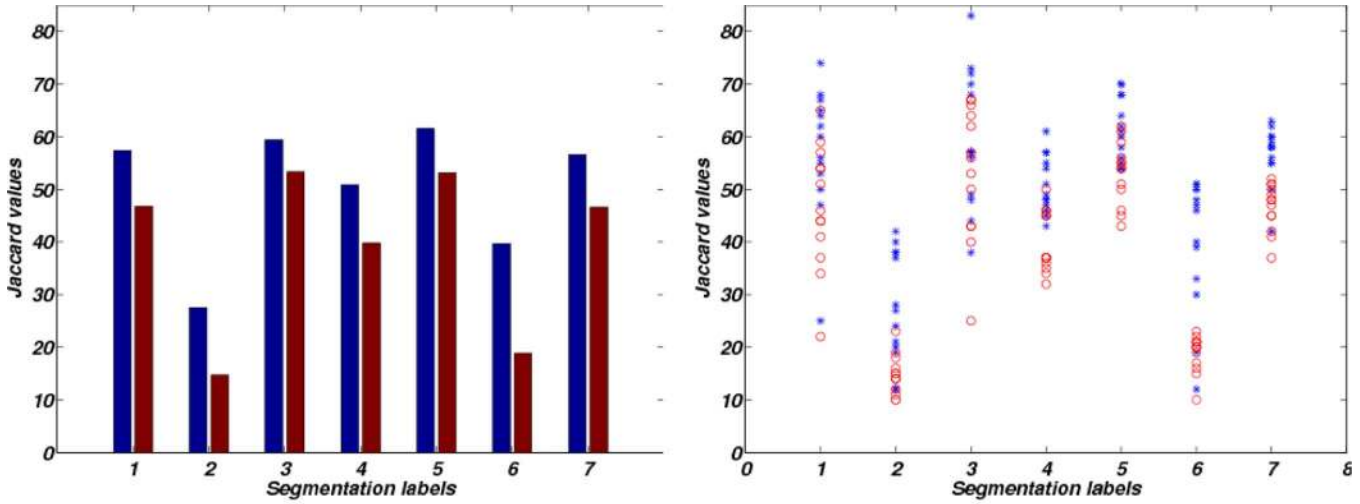

Fig. 9. Plots of jaccard values for different segmentation labels enumerated as 1:L-Vent, 2:L-CSF, 3:TUM, 4:L-GM, 5:G-Vent, 6:G-CSF, 7:G-GM. Left: mean values. Right: scattered samples. The red and blue colors correspond to ORBIT and our method's result.

TABLE VI
MEAN JACCARD VALUES OF DIFFERENT SEGMENTATION LABELS. SIGNIFICANT DIFFERENCES ARE INDICATED IN BOLD (P-VALUE ≤ 0.05)

Label	Our proposed method	ORBIT
L-Vent	**57.38**	46.77
L-CSF	**28.54**	15.69
TUM	59.38	53.31
L-GM	**50.85**	39.77
G-Vent	**62.54**	53.15
G-CSF	**40.0**	18.85
G-GM	**57.0**	47.62

our method clearly shows infiltration, and registered template resembles the patient image. The second example, indicates a case where the infiltration and the mass effect have been underestimated by ORBIT, whereas using our method the target tumor and the mass effect have been captured in a better way. The third and forth (separated by white spaces from top) samples in Fig. 10 indicate patients with lower grades of gliomas and smaller tumor bulks. The axial and sagital slices of the third and forth cases in (c), shows the ORBIT's failure to capture some parts of the tumor (as no tumor label is observed in the corresponding slice), whereas the result of our method shows some tumor diffusion, matching corresponding reference tumor PBM and a better registration performance has been achieved using our method (sample locations have been marked in the first column).

The first three rows on the top of Fig. 11 show an example patient, in which the ventricles have been heavily involved. As seen, ORBIT fails to capture the tumor pattern correctly, as the ventricles are not squeezed by its estimated tumor, whereas our method has a better performance since the created tumor resembles the patients tumor and ventricles indicate the mass effect. In the last example Fig. 11 (bottom rows), tumor is less infiltrative and has a bulk specified by the enhancement in the borders. ORBIT has over estimated the mass-effect and excessively pushed the ventricles, whereas such a pattern is not observed in our result and the ventricles are more similar to those of the patient.

VII. CONCLUSION AND FUTURE RESEARCH ORIENTATION

A deformable registration algorithm for glioma images with a normal atlas(template) is proposed. We utilized multiparametric imaging techniques to compute the tissue probability maps of the patient with an expert trained support vector machine. This step was critical to provide matching information on and around the tumor. Using fuzzy probabilistic maps is also especially important for gliomas, because those tumors are diffusive and therefore every voxel is expected to include some tumor portion. On the atlas, we used reaction-diffusion equation to simulate a tumor growth and estimate the mass-effect. Normal probability maps of the healthy atlas, were modified to reflect the tumor invasion, and registered to their corresponding probability maps in the patient image. In the atlas, since we do not model the edema, which is assumed to be confined into the white matter, the edema's probability map (PBM) remains as an unobserved additive component with the simulated white matter PBM. Therefore in edema region, the information of the white matter PBM is ignored and the registration is achieved by matching of CSF, gray matter and tumor PBMs between the patient and the tumor embedded atlas. Therefore we believe that the registration quality is better than the case in which the whole edema region is masked out from driving the registration ([23] and [24]). Such unrealistic modeling issues such as the lack of edema in the estimated PBMs on the atlas, is handled using EM algorithm, that estimates the spatial transformation and simultaneously segments the edema in the patient image.

The tumor parameters such as seed location, mass-effect coefficients, proliferation coefficient and diffusion parameters are estimated through APPSPACK [41]. The performance of the method was evaluated using both statistically simulated brain images, with known deformation field, and the real glioma images. Our experiments show that the proposed method has a very good registration performance, and the warped atlas resembles the target patient images.

To be accurate on registration errors, we used statistically simulated brain images and PBMs as target patient images. This allowed us to compare our computed deformation fields to

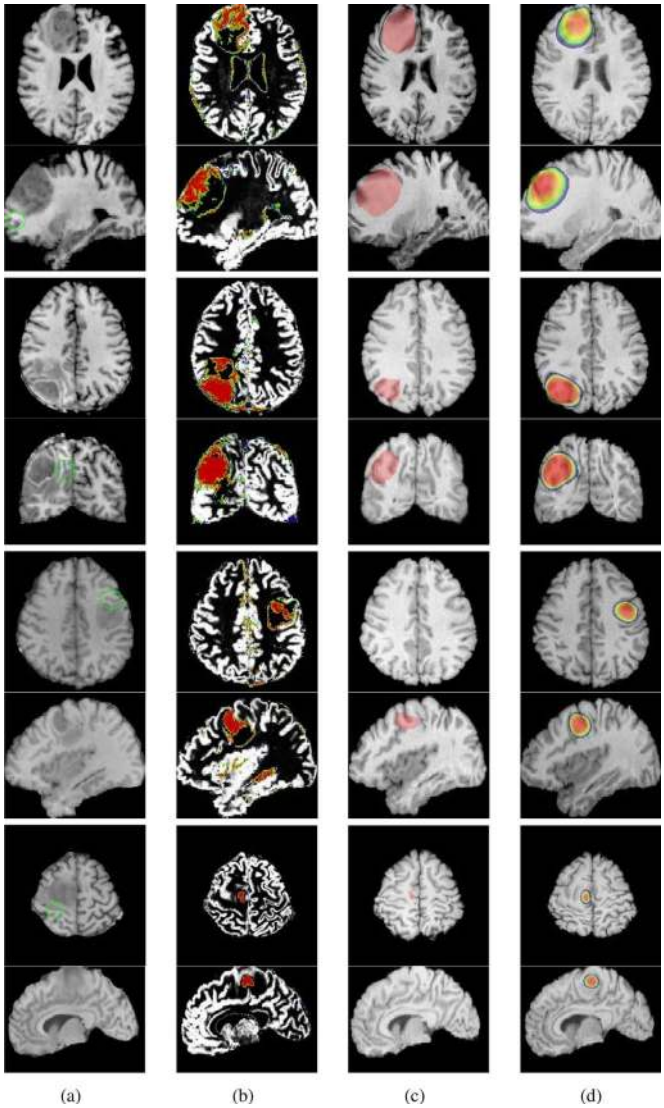

Fig. 10. Registration results with the same atlas shown in Fig. 3(a). The blank spaces in between the rows separates the patients. Columns from left to right: (a) T1 fixed reference images. (b) Overlay of the extracted PBMs of GM and TUM. (c) Warped template images to the reference using ORBIT (overlayed by the estimated tumor label). (d) Warped template using our algorithm (overlayed by the warped tumor density map originally generated in the atlas space). The markers in the first column around the tumor indicate some location where our method has had a better performance in comparison to ORBIT.

the ground truth deformations, available from our simulations. Table III summarizes mean square error results, and indicates the average of registration accuracy is in the order of one voxel size.

Comparison was made to ORBIT [19], this comparison was chosen especially because, for tumor images ORBIT has shown to outperform other registration methods. Both of our qualitative and quantitative results indicate that our method has a better performance, especially for highly infiltrated tumors. Examples for this claim can be found in Figs. 10 and 11, where some tumors indicate significant infiltration.

For real glioma images, our quantitative comparison of registration efficiency was based on the tissue overlap ratios as utilized in [47] and [48]. Jaccard ratio was especially preferred mainly because it allows rater independent evaluation of registration, and the complexity of the images did not allow reliable

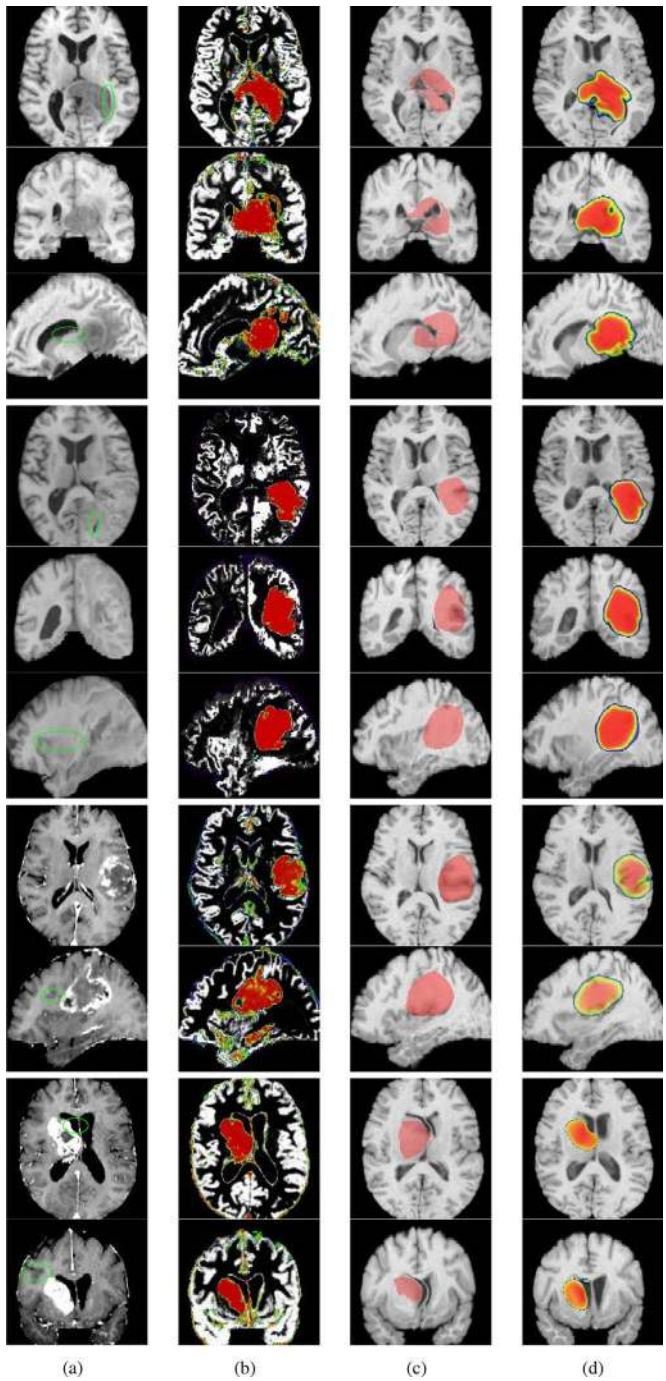

Fig. 11. Registration results with the same atlas shown in Fig. 3(a). The blank spaces in between the rows separates the patients. Columns from left to right: (a) T1 fixed reference images. (b) Overlay of the extracted PBMs of GM and TUM. (c) Warped template images to the reference using ORBIT (overlayed by the estimated tumor label). (d) Warped template using our algorithm (overlayed by the warped tumor density map originally generated in the atlas space). The markers in the first column around the tumor indicate some location where our method has had a better performance in comparison to ORBIT.

landmark localization. To be more specific, JRs were measured in both local (with respect to tumor) and global (considered as healthy) regions as shown in Table VI. The table demonstrates that our proposed method has a better performance compared to ORBIT. It should be pointed out that the main objective of such table is to establish a basis for the comparison and the

reported values can be further improved upon having a better quality on SVM classifier. In particular, poor overlap ratio on CSF, is partly because those structures are very tiny and therefore the overlap ratio is sensitive to small displacements. From our t-test scores, we notice that the improvement of registration in areas close to tumor was not equally significant as the rest of the brain. This is because, the current tumor growth models employed in both registration methods, have a limited ability to simulate anisotropic tumor patterns as they are observed in real glioma images. Such inadequately realistic tumor simulation causes poor matches and therefore although we have achieved an improvement (6%) over ORBIT, the difference is not statistically significant. In fact, the performance of the proposed method depends on the target tumor shape of the patient, and is the best for blob-like tumors. We expect upon integration of a better modeling, e.g., by fusion of DTI tensors for anisotropic tumor propagation along the white matter fiber tracts as done in [21], the quality of the registration to improve.

In addition, the current framework does not consider patients with multiple tumor bulks. In reality, metastasis might occur in glioma which results in several disjointed tumor areas. For such cases, several tumor seeds can be embedded in the atlas, however, this increases the number of parameters to be estimated and can result in a significantly longer processing time.

Although not covered in this paper, the sensitivity analysis of the registration quality with respect to patient PBMs is an important issue that should be addressed. We acknowledge that having a robust and accurate classification of the patient images, increases the registration quality. However, for noisy segmentations a compromise between the robustness and sensitivity of the algorithm can be established by adjusting the λ.[6]

One limitation in computing tissue probability maps is that, the current imaging modalities have intrinsic limitation to detect lower tumor cell densities [49], [50]. As a result, we acknowledge that with current modalities the computed PBMs on infiltrated areas might not be accurate. One interesting branch of future research is to enhance the accuracy of the measured PBMs by fusion of other information sources such as spectroscopies made around the tumor.

In the current form of our work, the edema is not directly simulated, mainly because it contributes to more complexity of our simulations, and increases the number of total required parameters, which would increase the computational cost in turn. Integration of edema modeling (such as one proposed by Nagashima *et al.* [39]) can be considered in the next steps. Also in the current implementation, the classification of the subject multimodality images is not updated during the registration process. Given an estimate of the registration of the atlas and tumor parameters, one can consider further refining the classification of the subject. The natural way for that purpose is to update the segmentation labels in the E step of our algorithm. This extension, however, was not initially considered since we wanted to favor the user's knowledge to be more specific on making segmentations of tumor and edema. The developed registration package is available for download via the homepage of Section of Biomedical Image Analysis, University of Pennsylvania (https://sbia-svn.uphs.upenn.edu/).

[6]To see this, note that regions with incorrect segmentation labels result in poor match to atlas and therefore are captured as outliers where $w_{i0}^{(m-1)}, w_{i1}^{(m-1)} \approx 0$, and $\|\mathbf{v}_i\| \approx 0$. In such locations the registration is driven by the neighborhood information. Since $w_{i0}^{(m-1)}, w_{i1}^{(m-1)}$ are inversely proportional to λ, increasing the λ makes the registration more robust but less sensitive (with respect to patient PBMs).

APPENDIX
PROOF OF UPDATE (18)

To compute the derivative according to (17), we first compute the differential with respect to $\mathbf{h}(\mathbf{x_i})$ and keep variances σ_i fixed at the current estimate, i.e., $\sigma_i = \sigma_i^{(m-1)}$. We only consider those terms in (15) which involve $\mathbf{h}(\mathbf{x_i})$

$$Q^{\mathbf{q}}(\Phi|\Phi^{(m-1)}) = \sum_{i=1}^{N}\Big\{ w_{i0}^{(m-1)} \left(\mathbf{y_i^q}\right)^t \left(\mathbf{S_0}^{(m-1)}\right)^{-1} \mathbf{y_i^q} + w_{i1}^{(m-1)} \left(\mathbf{y_i^q}\right)^t \left(\mathbf{S_1}^{(m-1)}\right)^{-1} \mathbf{y_i^q} \Big\} \quad (30)$$

by rearranging the terms

$$Q^{\mathbf{q}}(\Phi|\Phi^{(m-1)}) = \sum_{i=1}^{N}\Big\{ \left(\mathbf{y_i^q}\right)^t \Big[w_{i0}^{(m-1)} \left(\mathbf{S_0}^{(m-1)}\right)^{-1} + w_{i1}^{(m-1)} \left(\mathbf{S_1}^{(m-1)}\right)^{-1} \Big] \mathbf{y_i^q} \Big\}. \quad (31)$$

Let

$$\mathbf{R}_i^{(m-1)} = \left[w_{i0}^{(m-1)} \left(\mathbf{S_0}^{(m-1)}\right)^{-1} + w_{i1}^{(m-1)} \left(\mathbf{S_1}^{(m-1)}\right)^{-1} \right]$$

using the definition of directive differential operator $\langle \cdot, \cdot \rangle$ in (17) and its linear properties we have

$$\langle \partial Q^{\mathbf{q}}(\Phi|\Phi^{(m-1)}), \boldsymbol{\psi} \rangle = \sum_{i=1}^{N} \left\langle \left(\mathbf{y_i^q}\right)^t \mathbf{R}_i^{(m-1)} \mathbf{y_i^q}, \mathbf{v_i} \right\rangle$$

and using (20)

$$\begin{aligned} &\left\langle (\mathbf{y_i^q})^t \mathbf{R}_i^{(m-1)} \mathbf{y_i^q}, \mathbf{v_i} \right\rangle \\ &= \left(\mathbf{y_i^{q(m-1)}} + \left(\nabla \mathbf{M} \circ \mathbf{h}_i^{(m-1)} \right)^t \mathbf{v_i} \right)^t \\ &\times \mathbf{R}_i^{(m-1)} \left(\mathbf{y_i^{q(m-1)}} + \left(\nabla \mathbf{M} \circ \mathbf{h}_i^{(m-1)} \right)^t \mathbf{v_i} \right) \\ &- \left(\mathbf{y_i^{q(m-1)}} \right)^t \mathbf{R}_i^{(m-1)} \mathbf{y_i^{q(m-1)}} \end{aligned} \quad (32)$$

where $\nabla \mathbf{M}$ has been defined in (20). Keeping terms with up to the second order of $\|\mathbf{v}_i\|$, (32) can be summarized as

$$\begin{aligned} &\left\langle \left(\mathbf{y_i^q}\right)^t \mathbf{R}_i^{(m-1)} \mathbf{y_i^q}, \mathbf{v_i} \right\rangle \\ &= \mathbf{v_i}^t \Big[2 \nabla \mathbf{M} \circ \mathbf{h}_i^{(m-1)} \mathbf{R}_i^{(m-1)} \mathbf{y_i^{q(m-1)}} \\ &\quad + \nabla \mathbf{M} \circ \mathbf{h}_i^{(m-1)} \mathbf{R}_i^{(m-1)} \left(\nabla \mathbf{M} \circ \mathbf{h}_i^{(m-1)} \right)^t \mathbf{v_i} \Big]. \end{aligned} \quad (33)$$

Replacing (33) in (32), the right-hand side of (17) can be written as

$$\langle \partial Q^{\mathrm{q}}(\Phi|\Phi^{(m-1)}), \boldsymbol{\psi} \rangle = \sum_{i=1}^{N} \mathbf{v_i}^t . \left\{ \mathbf{r}_i^{(m-1)} + \mathbf{W}_i^{(m-1)} . \mathbf{v}_i \right\} = 0 \tag{34}$$

where $\mathbf{W}_i^{(m-1)}$ and $\mathbf{r}_i^{(m-1)}$, have the same definitions in (19)–(21). Since for every test function ψ defined in Ω_F the above equality should hold true we must have

$$\mathbf{r}_i^{(m-1)} + \mathbf{W}_i^{(m-1)} . \mathbf{v}_i = 0 \tag{35}$$

which is solved for the $\mathbf{v}_i$.

ACKNOWLEDGMENT

The authors would like to thank Dr. C. Hogea for developing the reaction-diffusion model, Dr. E. I. Zacharaki for helping us to run ORBIT and Dr. E. R. Melhem from the Department of Radiology, University of Pennsylvania, for providing us the patient's data sets.

REFERENCES

[1] S. Larjavaara, R. Mäntylä, T. Salminen, H. Haapasalo, J. Raitanen, J. Jääskeläinen, and A. Auvinen, "Incidence of gliomas by anatomic location," *Neuro. Oncol.*, vol. 9, pp. 319–325, 2007.

[2] H. Duffao and L. Capalle, "Preferential brain locations of low grade gliomas," *Cancer*, vol. 15, pp. 2622–2626, 2004.

[3] J. Ashburner and K. J. Friston, "Voxel-based morphometry: The methods," *NeuroImage*, vol. 11, pp. 805–821, 2000.

[4] G. E. Christensen and H. J. Johnson, "Consistent image registration," *IEEE Trans. Med. Imag.*, vol. 20, no. 7, pp. 568–582, Jul. 2001.

[5] H. L. Chui and A. Rangarajan, "A new point matching algorithm for non-rigid registration," *Comput. Vis. Image Understand.*, vol. 89, pp. 114–141, 2003.

[6] C. Davatzikos, "Spatial transformation and registration of brain images using elastically deformable models," *Comput. Vis. Image Understand.*, vol. 66, pp. 207–222, 1997.

[7] M. Ferrant, S. Warfield, C. Guttman, R. Mulkern, F. Jolesz, and R. Kikinis, "3-d image matching using a finite element based elastic deformation model," in *Proc. MICCAI*, 1999, pp. 202–209.

[8] J. C. Gee, "On matching brain volumes," *Pattern Recognit.*, vol. 32, pp. 99–111, 1999.

[9] H. J. Johnson and G. E. Christensen, "Consistent landmark and intensity-based image registration," *IEEE Trans. Med. Imag.*, vol. 21, no. 5, pp. 450–461, May 2002.

[10] S. Pizer, D. S. Fritsch, P. A. Yushkevich, V. E. Johnson, and E. L. Chaney, "Segmentation, registration and measurement of shape variation via image object shape," *IEEE Trans. Med. Imag.*, vol. 18, no. 10, pp. 851–865, Oct. 1999.

[11] D. Rueckert, L. I. Sonoda, C. Hayes, D. Hill, M. Leach, and H. Dj, "Nonrigid registration using free-form deformations: Application to breast MR images," *IEEE Trans. Med. Imag.*, vol. 18, no. 8, pp. 712–721, Aug. 1999.

[12] D. Shen and C. Davatzikos, "HAMMER: Hierarchical attribute matching mechanism for elastic registration," *IEEE Trans. Med. Imag.*, vol. 21, no. 11, pp. 1421–1439, Nov. 2002.

[13] C. Studholme, V. Cardenas, K. Blumenfeld, N. Schuff, H. J. Rosen, and B. M. Weiner, "Deformation tensor morphometry of sematic dementia with quantitive validation," *NeuroImage*, vol. 21, pp. 1387–1398, 2004.

[14] P. Thompson and A. W. Toga, "A surface-based technique for warping three-dimensional images of the brain," *IEEE Trans. Med. Imag.*, vol. 15, no. 4, pp. 402–417, Aug. 1996.

[15] B. C. Vemuri, J. Ye, Y. Chen, and C. M. Leonard, "Image registration via level-set motion: Applications to atlas-based segmentation," *Med. Image Anal.*, vol. 7, pp. 1–20, 2003.

[16] J. P. Pluim, J. B. Maintz, and M. A. Viergever, "Mutual-information based registration of medical images: A survey," *IEEE Trans. Med. Imag.*, vol. 22, no. 8, pp. 986–1004, Aug. 2003.

[17] M. P. Lorenzen, B. Davis, G. Gerig, E. Bullitt, and S. Joshi, "Multimodal image set registration and atlas formation," *Med. Image Anal.*, vol. 10, pp. 440–451, 2006.

[18] E. I. Zacharaki, D. Shen, S. K. Lee, and C. Davatzikos, "ORBIT: A multiresolution framework for deformable registration of brain tumor images," *IEEE Trans. Med. Imag.*, vol. 27, no. 8, pp. 1003–1018, Aug. 2008.

[19] E. I. Zacharaki, C. S. Hogea, D. Shen, G. Biros, and C. Davatzikos, "Non-diffeomorphic registration of brain tumor images by simulating tissue loss and tumor growth," *Neuroimage*, vol. 46, pp. 762–774, 2009.

[20] C. Hogea, C. Davatzikos, and G. Biros, "An image-driven parameter estimation problem for a reaction-diffusion glioma growth model with mass effects," *J. Math. Biol*, vol. 56, pp. 793–825, 2008.

[21] O. Clatz, M. Sermesant, P. Y. Bondiau, H. Delingette, S. K. Warfield, G. Malandain, and N. Ayache, "Realistic simulation of the 3-d growth of brain tumors in MR images coupling diffusion with mass effect," *IEEE Trans. Med. Imag.*, vol. 24, no. 10, pp. 1334–1346, Oct. 2005.

[22] C. S. Hogea, F. Abraham, G. Biros, and C. Davatzikos, "A framework for soft tissue simulations with applications to modeling brain tumor mass-effect in 3-d images," in *Proc. 3rd Canadian Conf. Comput. Rob. Vis. (CRV)*, 2006, pp. 24–33.

[23] M. Brett, A. P. Leff, C. Rorden, and J. Ashburner, "Spatial normalization of brain images with focal lesions using cost function masking," *Neuroimage*, vol. 14, pp. 486–500, 2001.

[24] R. Stefanescu, O. Commowick, G. Malandain, P. Y. Bondiau, N. Ayache, and X. Pennec, "Non-rigid atlas to subject registration with pathologies for conformal brain radiotherapy," in *In Proc.MICCAI*, 2004, pp. 704–711.

[25] W. L. Nowinski and D. Belov, "Toward atlas-assisted automatic interpretation of MRI morphological brain scans in the presence of tumor," *Acad. Radiol.*, vol. 12, pp. 1049–1057, 2005.

[26] S. K. Kyriacou, C. Davatzikos, S. J. Zinreich, and R. N. Bryan, "Nonlinear elastic registration of brain images with tumor pathology using a biomechanical model," *IEEE Trans. Med. Imag.*, vol. 18, no. 7, pp. 580–592, Jul. 1999.

[27] K. A. Ganser, H. Dickhausa, R. Metznerb, and C. R. Wirtzb, "A deformable digital brain atlas system according to talairach and tournoux," *Med. Image Anal.*, vol. 8, pp. 3–22, 2004.

[28] M. B. Cuadra, C. Pollo, A. Bardera, O. Cuisenaire, J. G. Villemure, and J. P. Thiran, "Atlas-based segmentation of pathological MR brain images using a model of lesion growth," *IEEE Trans. Med. Imag.*, vol. 23, no. 10, pp. 1301–1314, Oct. 2004.

[29] B. M. Dawant, S. L. Hartmann, and S. Gadamsetty, "Brain atlas deformation in the presence of large space-occupying tumours," in *Proc. MICCAI*, 1999, vol. 1679, pp. 589–596.

[30] M. B. Cuadra, M. Craene, V. Duay, B. Macq, C. Pollo, and J. P. Thiran, "Dense deformation field estimation for atlas-based segmentation of pathological MR brain images," *Comput. Methods Programs Biomed.*, vol. 84, pp. 66–75, 2006.

[31] A. Mohamed, E. I. Zacharaki, D. Shen, and C. Davatzikos, "Deformable registration of brain tumor images via a statistical model of tumor-induced deformation," *Med. Image Anal.*, vol. 10, pp. 752–763, 2006.

[32] A. Mohamed and C. Davatzikos, "Finite element modeling of brain tumor mass-effect from 3-d medical images," in *Proc. MICCAI*, 2005, pp. 400–408.

[33] R. Verma, E. I. Zacharaki, Y. Ou, H. Cai, S. Chawla, S. K. Lee, E. R. Melhem, and R. W. Davatzikos, "Multiparametric tissue characterization of brain neoplasms and their recurrence using pattern classification of MR images," *Acad. Radiol.*, vol. 15, pp. 566–977, 2008.

[34] W. Stummer, "Mechanisms of tumor-related brain edema," *Neurosurgical FOCUS*, pp. 1–7, 2007.

[35] C. Hogea, C. Davatzikos, and G. Biros, "Brain tumor interaction biophysical models for medical image registration," *SIAM. J. Sci. Comput*, vol. 30, pp. 3050–3072, 2008.

[36] K. R. Swanson, E. Jr, and D. Murray, "A quantitative model for differential motality of gliomas in grey and white matter," *Cell Prolif.*, vol. 33, pp. 317–329, 2000.

[37] Y. Zhang, M. Brady, and S. Smith, "Segmentation of brain MR images through a hidden Markov random field model and the expectation maximization algorithm," *IEEE Trans. Med. Imag.*, vol. 20, no. 1, pp. 45–57, Jan. 2001.

[38] C.-C. Chang and C.-J. Lin, LIBSVM: A library for support vector machines 2001 [Online]. Available: http://www.csie.ntu.edu.tw/cjlin/libsvm

[39] T. Nagashima, N. Tamaki, M. Takada, and Y. Tada, "Formation and resolution of brain edema associated with brain tumors: A comprehensive theoretical model and clinical analysis," *Acta Neurochir. Suppl. (Wien)*, vol. 60, pp. 165–167, 1994.

[40] M. Prastawa, E. Bullitt, N. Moon, K. V. Leemput, and G. Gerig, "Automatic brain tumor segmentation by subject specific modification of atlas priors," *Acad. Radiol.*, vol. 10, pp. 1341–1348, 2003.

[41] J. D. Griffin and T. G. Kolda*, Asynchronous Parallel Generating Set Search for Linearly-Constrained Optimization*. Albuquerque, NM: Sandia National Laboratories, 2006.

[42] K. V. Leemput, F. Maes, F. Bello, D. Vandermeulen, A. Colchester, and P. Suetens, "Automated segmentation of multiple sclerosis lesions by model outlier detection," *IEEE Trans. Med. Imag.*, vol. 20, no. 8, pp. 677–688, Aug. 2001.

[43] J. P. Thirion, "Image matching as diffusion process: An analogy with maxwell's demons," *Med. Ima. Anal.*, vol. 2, pp. 243–260, 1998.

[44] T. Vercauteren, X. Pennec, A. Perchant, and N. Ayache, "Diffeomorphic demons: Efficient non-parametric image registration," *Neuroimage*, vol. 45, pp. 61–72, 2009.

[45] M. Jenkinson, P. R. Bannister, J. M. Brady, and S. M. Smith, "Improved optimization for the robust and accurate linear registration and motion correction of brain images," *Neuroimage*, vol. 17, pp. 825–841, 2002.

[46] X. Zhong, S. Dinggang, K. Bilge, and D. Christos, "Statistical representation and simulation of high-dimensional deformations: Application to synthesizing brain deformations," in *Proc. MICCAI*, 2005, pp. 500–508.

[47] G. Postelnicu, L. Zollei, and B. Fischl, "Combined volumetric and surface registration," *IEEE Trans. Med. Imag.*, vol. 28, no. 4, pp. 508–522, Apr. 2008.

[48] W. R. Crum, D. Rueckert, M. Jenkinson, D. Kennedy, and S. M. Smith, "A framework for detailed objective comparison of non-rigid registration algorithms in neuroimaging," in *Proc. MICCAI*, 2004, pp. 679–686.

[49] E. Konukoglu, O. Clatz, P. Y. Bondiau, H. Delingette, and N. Ayache, "Extrapolating glioma invasion margin in brain magnetic resonance images: Suggesting new irradiation margins," *Med. Image Anal.*, vol. 14, no. 2, pp. 111–125, 2010.

[50] P. Tracqui *et al.*, "A mathematical model of glioma growth: The effect of chemotherapy on spatio-temporal growth," *Cell Prolif.*, vol. 28, pp. 17–31, 1995.